On vectorial integer bootstrapping implementations in the estimation of satellite orbits and clocks based on small global networks

Massarweh, Lotfi; Strasser, Sebastian ; Mayer-Gürr, Torsten

DOI
10.1016/j.asr.2021.09.023

Publication date
2021

Document Version
Final published version

Published in
Advances in Space Research

Citation (APA)
Massarweh, L., Strasser, S., & Mayer-Gürr, T. (2021). On vectorial integer bootstrapping implementations in the estimation of satellite orbits and clocks based on small global networks. *Advances in Space Research*, *68*(11), 4303-4320. https://doi.org/10.1016/j.asr.2021.09.023

Available online at www.sciencedirect.com

ScienceDirect

Advances in Space Research 68 (2021) 4303–4320

ADVANCES IN SPACE RESEARCH (a COSPAR publication)

www.elsevier.com/locate/asr

On vectorial integer bootstrapping implementations in the estimation of satellite orbits and clocks based on small global networks

Lotfi Massarweh [a,*], Sebastian Strasser [b], Torsten Mayer-Gürr [b]

[a] Geoscience and Remote Sensing, Delft University of Technology, Stevinweg 1, 2628 CN Delft, Netherlands
[b] Institute of Geodesy, Graz University of Technology, Steyrergasse 30, 8010 Graz, Austria

Received 22 June 2021; received in revised form 26 August 2021; accepted 22 September 2021
Available online 2 October 2021

Abstract

The estimation of satellite orbits and clocks plays a central role in different Global Navigation Satellite System (GNSS) domains, e.g. precise positioning or time transfer. Such products can be computed in the process of Orbit Determination and Time Synchronization (ODTS), which relies on a network of ground-based stations, well distributed around the globe. The mm-level precision of carrier-phase measurements is exploited in this network estimation following a correct resolution of their ambiguities. For several stations, satellites and/or signals, thousands of ambiguities have to be processed, which means having to deal with high-dimensional ambiguity resolution (HDAR) problems. In this research work, we firstly account for the impact of ambiguity resolution in a varying network size, based on GPS-only, Galileo-only and GPS+Galileo configurations. Using 25 or more stations, the accuracy (1D RMS orbital errors) of *fixed* solutions reaches a plateau at 1–2 cm. Hence, we focus on a small global network of 14 stations, where the model strength decreases, so does the reliability of the ambiguity fixing process and advantages over a *float* solution might become less evident. In order to allow reliable HDAR, two implementations of the Vectorial Integer Bootstrapping estimator are presented and evaluated with respect to their scalar counterpart. Finally, it is shown how the proposed fixing processes are more robust, still very efficient, and on certain days they provide a large improvement to satellite products. The orbital results are ultimately validated by considering the satellite midnight discontinuity errors over a 3-month period in 2019.

Keywords: Global Navigation Satellite System (GNSS); Vectorial Integer Bootstrapping (VIB); Ambiguity Resolution (AR); Orbit Determination and Time Synchronization (ODTS)

1. Introduction

The generation of satellite orbit and clock information represents an essential element for any Regional/Global Navigation Satellite System (RNSS/GNSS) and is generally based on the use of code and phase observations from a ground-based network of station receivers. The so-called process of Orbit Determination and Time Synchronization (ODTS) makes the best use of state-of-the-art knowledge on orbital dynamics for all tracked satellites (Montenbruck and Steigenberger, 2020). This a priori information can be consequently improved by means of an accurate functional and stochastic modeling of such measurements, ideally consistent with the models later adopted on the user side.

The contribution of carrier-phase measurements, very precise but ambiguous, is a key aspect in the network estimation, whether a global or a regional one. In fact, to exploit their mm-level precision, the integer ambiguities need to be correctly resolved, which is not an easy task when dealing with global networks (Ge et al., 2006). Given

* Corresponding author.
E-mail addresses: L.massarweh@tudelft.nl (L. Massarweh), sebastian.strasser@tugraz.at (S. Strasser), mayer-guerr@tugraz.at (T. Mayer-Gürr).

https://doi.org/10.1016/j.asr.2021.09.023
0273-1177/

denser networks, many satellites from different GNSS constellations and/or multi-frequency signals, the number of ambiguity components grows rapidly, along with the complexity of the integer ambiguity resolution (IAR). This leads to the necessity for a balanced trade-off between *efficiency* and *robustness* of the IAR process, for example in support of a low-latency generation of precise satellite orbits and clocks products.

Simple and intuitive strategies can be used (Blewitt, 1989; Cocard and Geiger, 1992), e.g. well-known widelaning approaches, but sophisticated ones are available. For instance, the Least-squares AMBiguity Decorrelation Adjustment (LAMBDA) method, introduced in Teunissen (1995), which provides an effective solution to the IAR. The LAMBDA approach enables the adoption of a wide range of possible estimators, suitable for both low and high accuracy applications, and it has been proved to be relatively efficient up to a few hundred ambiguity components (Li and Teunissen, 2011). Expected performances for precise long-baseline positioning using both GPS and Galileo are presented in Odijk et al. (2014) based on a formal analysis, for instance in terms of predicted success rate. The advantages when considering GPS+Galileo have been further investigated (Nardo et al., 2016), where different long baseline scenarios (ground- and space-based) are simulated and examined.

However, nowadays, we might deal with problems of a much larger dimensionality (Chen et al., 2014), where thousands of ambiguity components are involved, and the overall complexity grows exponentially in such a "dimensional curse" (Verhagen et al., 2012b). This dimensionality aspect might lead to a computational bottleneck (Jazaeri et al., 2012), and the high-dimensional ambiguity resolution (hereinafter HDAR) problems are less likely solvable in a reliable way and within short computational times.

In this work, we consider the Vectorial Integer Bootstrapping (VIB) estimator described in Teunissen et al., 2021. The flexibility of such a VIB formulation allows for an arbitrary partitioning of the original n-dimensional ambiguity problem, along with a suitable choice of the integer estimator in use. Two (possible) implementations are described: firstly, a straightforward Cascade AR (CascAR) algorithm and secondly, a blocked search approach in use by Graz University of Technology (TUG). Both the two algorithms are shown to be efficiently constructed starting from the same triangular decomposition, while following LAMBDA decorrelation of ambiguities.

Using the ODTS strategy and software developed at Graz University of Technology (Strasser et al., 2019), we analyze different network configurations in order to further define the impact of ambiguity resolution with respect to the network size. The latter is assessed by looking at the accuracy of satellite products. We focus on a small global network, where the correct ambiguity resolution shows to provide the most benefits, e.g. in terms of orbital errors. The two VIB implementations are validated over a 3-month period in 2019, using GPS+Galileo real data from a network of 14 well-distributed stations. Both these VIB-based approaches show the great convenience of this easy-to-implement and flexible formulation, while also leaving room for improvement. In fact, more advanced algorithms might be designed ad hoc in several GNSS domains, not limited to this network case.

In Section 2, the two algorithms are introduced as examples of implementation for the VIB estimator. In Section 3, the network estimation strategy for satellite orbits and clocks is delineated, along with configurations and a few scenarios considered in this work. The main results are presented and analyzed within Section 4, focusing on a small global network and also briefly comparing the two algorithms. In Section 5, we perform an extensive validation over a 3-month period, followed by a short discussion on this vectorial formulation. Lastly, in Section 6, the overall conclusions are given.

2. Integer ambiguity resolution methodology

We start from a linear(ized) mixed-integer GNSS model estimation (Leick et al., 2015), given the vector of code and phase observations as $y \in \mathbb{R}^m$ with its positive-definite variance-covariance (vc-) matrix as $Q_{yy} \in \mathbb{R}^{m\times m}$, such that

$$\mathrm{E}\{y\} = Aa + Bb, \quad \mathrm{D}\{y\} = Q_{yy} \tag{1}$$

with $\mathrm{E}\{\cdot\}$ and $\mathrm{D}\{\cdot\}$ being the expectation and dispersion operators, respectively. The matrix $(A, B) \in \mathbb{R}^{m\times(n+p)}$ denotes a full-rank design matrix, with $a \in \mathbb{Z}^n$ as vector of carrier-phase integer ambiguity and $b \in \mathbb{R}^p$ as vector of real-valued parameters. The latter refer, without loss of generality, to estimable parameters in the ODTS process, for example satellite orbit and clock products, as later discussed in Section 3.

By means of an orthogonal decomposition (Teunissen, 1993), we can separate the quadratic objective function (with integerness constraints) into a sum of three squares as

$$\|y - Aa - Bb\|^2_{Q_{yy}} = \|\hat{e}\|^2_{Q_{yy}} + \|\hat{a} - a\|^2_{Q_{\hat{a}\hat{a}}} + \|\hat{b}(a) - b\|^2_{Q_{\hat{b}(a)}} \tag{2}$$

where $\|\blacksquare\|^2_Q = (\blacksquare)^T Q^{-1}(\blacksquare)$ refers to a squared Mahalanobis distance (Mahalanobis, 1936), i.e. a weighted norm in the metric given by Q^{-1}. This previous decomposition leads to a subsequent three-step minimization of the original objective function.

In the first step, $\hat{e} \in \mathbb{R}^m$ is the residual vector of a least-squares solution that neglects the integerness constrains on ambiguities. These estimated (float) ambiguities $\hat{a} \in \mathbb{R}^n$, and their vc-matrix $Q_{\hat{a}\hat{a}} \in \mathbb{R}^{n\times n}$, are therefore used in a second step to solve an Integer Least Squares (ILS) problem, e.g. considering a many-to-one map $\mathcal{I} : \mathbb{R}^n \to \mathbb{Z}^n$, such that their integer-fixed estimate is $\check{a} = \mathcal{I}(\hat{a})$. Given that no constrains are taken into account for b, a fixed solution to the third step is easily found by considering

$b = b(\check{a}) \overset{\text{def}}{=} b - Q_{\hat{b}\hat{a}}Q_{\hat{a}\hat{a}}^{-1}(\hat{a} - \check{a})$ and, for $Q_{\hat{a}\hat{a}} \approx 0$ (Verhagen, 2004), we can safely assume $Q_{\check{b}\check{b}} \approx Q_{\hat{b}\hat{b}} - Q_{\hat{b}\hat{a}}Q_{\hat{a}\hat{a}}^{-1}Q_{\hat{a}\hat{b}}$.

A focal point in this three steps process becomes the minimization of $\|\hat{a} - a\|^2_{Q_{\hat{a}\hat{a}}}$, which can still be tackled by different classes of estimators, i.e. Integer (I) estimators (Teunissen, 1999), Integer Aperture (IA) estimators (Teunissen, 2003a) or Integer Equivariant (IE) estimators (Teunissen, 2002). These three classes are proper subsets of one another, thence $I \subset IA \subset IE$, with the I- and IE-class being the smallest and largest, respectively. Further mathematical details are summarized and extensively discussed in Teunissen (2003b).

2.1. Review of Vectorial Integer Bootstrapping estimators

The Vectorial Integer Bootstrapping (VIB) method, defined in Teunissen et al., 2021, hinges on a further orthogonal decomposition of the second term in Eq. (2). In fact, it is possible to define an *arbitrary* partitioning of the initial vector $a \in \mathbb{Z}^n$, i.e. $a_1 \in \mathbb{Z}^{n_1}, a_2 \in \mathbb{Z}^{n_2}$, where all ambiguity components are still involved, so $n = n_1 + n_2$. It follows that

$$\min_{a\in\mathbb{Z}^n}\|\hat{a} - a\|^2_{Q_{\hat{a}\hat{a}}} = \min_{a_1\in\mathbb{Z}^{n_1}, a_2\in\mathbb{Z}^{n_2}}\left(\|\hat{a}_1(a_2) - a_1\|^2_{Q_{1|22}} + \|\hat{a}_2 - a_2\|^2_{Q_{22}}\right) \quad (3a)$$

$$\approx \min_{a_1\in\mathbb{Z}^{n_1}}\left(\|\hat{a}_1(a_2) - a_1\|^2_{Q_{1|22}}\right) + \min_{a_2\in\mathbb{Z}^{n_2}}\left(\|\hat{a}_2 - a_2\|^2_{Q_{22}}\right) \quad (3b)$$

for $Q_{11|22} = Q_{11} - Q_{12}Q_{22}^{-1}Q_{21}$ as Schur complement (Zhang, 2006) of block Q_{22} in $Q_{\hat{a}\hat{a}}$. The latter follows from a conformable blocks' partitioning, i.e. $Q_{12} \in \mathbb{R}^{n_1\times n_2}$, such as

$$Q_{\hat{a}\hat{a}} = \begin{bmatrix} Q_{11} & Q_{12} \\ Q_{12}^T & Q_{22} \end{bmatrix} \quad (4)$$

with $\hat{a}_1(a_2) = \hat{a}_1 - Q_{12}Q_{22}^{-1}(\hat{a}_2 - a_2)$ here referring to the float ambiguity subset 1 conditioned on 2. In the VIB approach, the first term in parenthesis for Eq. (3a) is then minimized only accounting for $a_1 \in \mathbb{Z}^{n_1}$, thus assuming in Eq. (3b) that a_2 is given from the second minimization, i.e. $\check{a}_2 = \mathcal{I}_2(\hat{a}_2)$ for an admissible integer mapping $\mathcal{I}_2 : \mathbb{R}^{n_2} \to \mathbb{Z}^{n_2}$.

The VIB solution is consequently suboptimal, and its success rate depends upon the ambiguity parametrization, as it does for its scalar counterpart (Teunissen, 1998). Still, the integer search is now performed over two smaller subsets rather than over a large domain, whose complexity increases exponentially with the n dimensionality (Brack, 2019). A similar principle is, nonetheless, also known in the *scalar* Integer Bootstrapping (IB) method, where the number of blocks m is equal to n, so having $n_i = 1, \forall i = 1, \ldots, m$. On the other hand, for $m = 1$ we have $n_1 = n$, and thence the overall ILS (optimal) solution is computed.

It is important to observe that each block is always conditioned on the previous ones, preferably going from the most to the least precise subset. This conditioning should not be neglected since it is a key aspect for improving the VIB success rate (Teunissen et al., 2021), and for the same parametrization it can lead to a solution that is closer to optimality than in the scalar IB case. In order to maximize the robustness of the fixing within each subset, all blocks are sequentially processed by means of an ILS estimator as discussed in the following sections.

2.2. Cascade Ambiguity Resolution (CascAR) algorithm

The CascAR algorithm is based on a quite general implementation of VIB estimators, and it allows having an efficient characterization of each subset, since it requires only a single L^TDL-decomposition of the (float) ambiguity vc-matrix. It follows as $Q_{\hat{a}\hat{a}} = L_{\hat{a}}^T D_{\hat{a}} L_{\hat{a}}$, where $L_{\hat{a}}, D_{\hat{a}} \in \mathbb{R}^{n\times n}$ are a lower unitriangular and a diagonal matrix, respectively. This triangular decomposition has a statistical interpretation, e.g. see Teunissen (1995), and it leads to the desired sum-of-blocks structure discussed in Section 2.1.

Given an arbitrary partitioning with m blocks, for $m \in [1, n]$, we can write

$$\|\hat{a} - a\|^2_{Q_{\hat{a}\hat{a}}} = \sum_{i=1}^{i=m}\|\hat{a}_{i|J} - a_i\|^2_{Q_{i|J}}, \quad J = \{i+1, \ldots, m\} \quad (5)$$

with the (conditioned) ambiguity subsets $\hat{a}_{i|J} \in \mathbb{R}^{n_i}$, for $n = n_1 + \ldots + n_m$. Furthermore, we set $\hat{a}_{m|J} = \hat{a}_m$, being the unconditioned block (i.e. firstly processed). In Teunissen et al., 2021, a block-decomposition is shown to define subsets, thus implying a certain selection for the partitioning, i.e. values n_i. Nonetheless, in a very similar way, the metric used in each sub-problem can be retrieved directly as $Q_{ii|J} = L_{ii}^T D_{ii} L_{ii}$, where a conformable (in size) partitioning of $L_{\hat{a}}, D_{\hat{a}}$ has been adopted. For the sake of clarity, additional mathematical details are given in Appendix A.

We can describe the CascAR algorithm (see Fig. 1) by assuming that ambiguities are firstly decorrelated with the LAMBDA software (Verhagen et al., 2012a) by means of a Z-transformation, for $Z \in \mathbb{Z}^{n\times n}$ (unimodular), such that $\hat{z} = Z^T\hat{a}$ and $Q_{\hat{z}\hat{z}} = Z^T Q_{\hat{a}\hat{a}} Z$. This "pre-processing" step enhances the success rate for our VIB solution, improves the integer search process, and it also assures that ambiguity components are sorted based on their precision. The latter is an important element since it is convenient to firstly fix very precise blocks (i.e. with a high success rate), so to later condition the remaining ones on these more reliably fixed blocks. In order to assure a full consistency with LAMBDA routines, the most precise components are set within the last block $i = m$, which is where we start. We then continue the cascade (conditioning) process to $i = m-1, m-2, \ldots$, till we reach $i = 1$.

The CascAR algorithm takes as inputs the triangular decomposition for a decorrelated ambiguity vc-matrix, i.e. $Q_{\hat{z}\hat{z}} = L_{\hat{z}}^T D_{\hat{z}} L_{\hat{z}}$, and a float vector $\hat{z}$ relative to the full set. Once the first partitioning has been defined by n_m, we

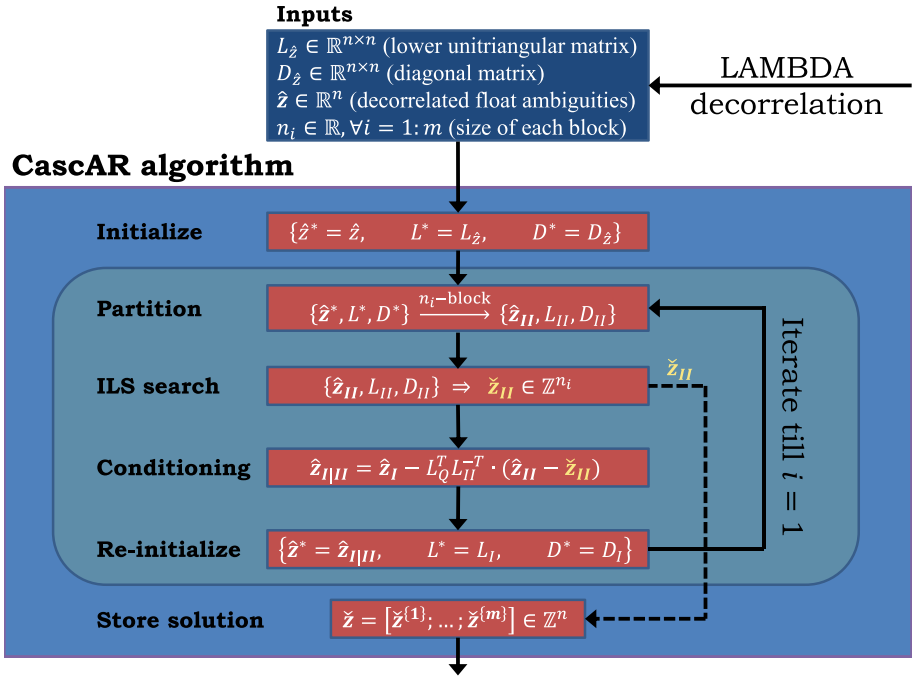

Fig. 1. The CascAR algorithm is shown, where the initial ILS problem can be partitioned into m blocks, starting from ambiguity components that have been previously decorrelated in LAMBDA.

initialize the aforementioned inputs with "*" and we divide the problem in two subsets I and II.

Hence, we get $\hat{z}_I \in \mathbb{R}^{n}_{I}$ and $\hat{z}_{II} \in \mathbb{R}^{n}_{II}$, where $n_I = n_1 + \ldots + n_{m-1}$ and $n_{II} = n_m$. This second block (presumed to be more precise) is processed in order to obtain an ILS solution $\check{z}_{II} \in \mathbb{Z}^{n}_{II}$, later adopted to condition the remaining ambiguities. We should observe that this conditioning operation takes place directly by means of conformable blocks in the matrix $L_{\hat{z}}$, so directly using $L_Q \in \mathbb{R}^{n_{II}\times n_I}$ and $L_{II} \in \mathbb{R}^{n_{II}\times n_{II}}$ (see details in Appendix A).

At the end of this first iteration, the block I is re-initialized with "*" and we re-iterate the process till $n_{II} = n_1$, while $n_I = 0$. During each i-th iteration, the integer-fixed solution $\check{z}^{\{i\}} \in \mathbb{Z}^{n_i}$ of the respective subset is stored in a single (column) vector $\check{z}_{\mathrm{VIB}}$, given as

$$\check{z}_{\mathrm{VIB}} = \begin{bmatrix} \check{z}^{\{1\}} \\ \vdots \\ \check{z}^{\{i\}} \\ \vdots \\ \check{z}^{\{m\}} \end{bmatrix} \in \mathbb{Z}^n \tag{6}$$

that still represents an integer solution to the problem as seen in Eq. (3b). The selection over number of blocks m and their respective dimensionality n_i is discussed in Section 3.2.1.

2.3. TUG's "blocked search" IAR method

When looking at vectorial approaches, there are several examples available in literature as highlighted in Teunissen et al., 2021. Another possible approach that can be placed within the family of VIB estimators is the so-called "blocked search" algorithm that has been firstly described in Strasser et al. (2019). It shows quite some similarities with the CascAR implementation, but with an alteration of the cascade processing.

This method considers overlapping blocks, de facto re-processing several components twice but as part of different subsets. The driving motivation is that the optimal solution for a certain ILS problem is unique, i.e. a definite n-dimensional set of integer ambiguities, and therefore fixed solutions for overlapping blocks should have the same integer components. If two adjacent blocks lead to different integer values for their overlapping components, then the integer search is performed over their joint subsets.

We should carefully consider that while this approach is not formally defined from a mathematical point of view, it still presents a quite interesting variation of the VIB approach and is therefore considered in this investigation. In Fig. 2 a schematic view of the TUG method is given for a simplified case, as a matter of example, based on a blocked partitioning of an ILS problem with $n = 400$, where each block involves 100 ambiguity components.

The TUG algorithm starts processing each 100-dimensional block in a main cascade and overlapping blocks (of same dimensionality) in a secondary one. When all integer-fixed components in common sub-blocks (i.e. here 50 ambiguities) are the same we obtain the respective fixed solution (in green color) for that portion of the block. When a different solution (in red color) is found between this main and secondary cascade, then the search is performed in the joint subset that contains 150 ambiguities.

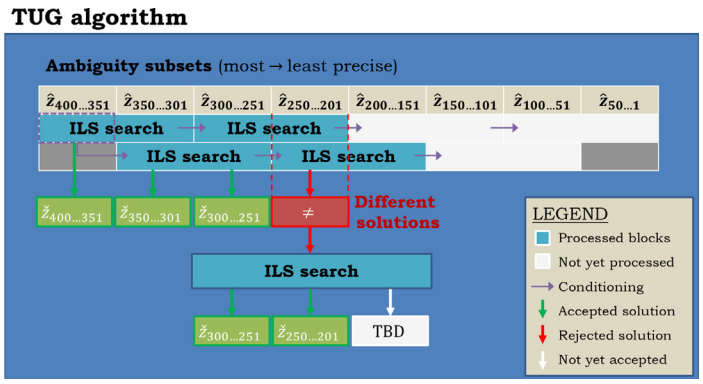

Fig. 2. The TUG algorithm is shown based on decorrelated ambiguities. The overlapping subsets are fixed and used to conditioning the following ones. See text for more details.

The solution of this larger integer search provides the 100 fixed components, including those 50 that differed originally, while the last 50 solution components are not yet accepted. In fact, these last 50 components overlap with a new block in the main cascade (i.e. from $\hat{z}_{200}$ till $\hat{z}_{101}$) that has not been processed yet. Once this block has been processed and the overlapping integer components match, we continue the process; otherwise the same "expansion and search" strategy is performed as before. Note that when working with such larger subsets, then we condition the successive ambiguities based on this new solution.

It is understandable that such an overlapping vectorial approach leads to higher computational times, since most components are processed twice. In addition to that, when rejections occur, we also deal with larger ILS problems. Increasing the dimensionality by 50% might lead (in some cases) to higher computational times, depending on the initially chosen size. Hence, it is also important to somehow limit the expansion strategy otherwise the entire process could become jammed in an interminable integer search process.

3. Processing strategy and scenarios selection

The experiments presented in this article are conducted using the open-source software GROOPS (Mayer-Gürr et al., 2021), which is developed and maintained at Graz University of Technology. The source code of GROOPS is available on GitHub (https://github.com/groops-devs/groops) together with documentation and an installation guide. The software features GNSS processing capabilities based on an implementation of the raw observation approach (Strasser et al., 2019). It supports multi-GNSS and multi-signal environments and is optimized for the processing of large GNSS station networks. GROOPS was used to process up to 800 stations and 75 GPS, GLONASS and Galileo satellites per day for TUG's contribution (Strasser and Mayer-Gurr, 2021) to IGS repro3, the third reprocessing campaign of the International GNSS Service (Johnston et al., 2017). GROOPS-based GNSS products are thus going to be incorporated into the next version of the International Terrestrial Reference Frame (i.e. ITRF2020).

The processing setup for the conducted experiments is similar to that of repro3 and generally follows what is documented in Strasser et al. (2019). All processing is performed in daily 24-h batches. The parameters estimated per day are listed in Table 1. The seven ECOM2 solar radiation pressure parameters are $\{D_0, D_{2C}, D_{2S}, Y_0, B_0, B_{1C}, B_{1S}\}$ (cf. Arnold et al. (2015)). Strasser et al. (2019) provides more detailed information on the parametrizations used for the different components, for example how the ionospheric influence is separated from code biases and clock errors. The estimated code and phase biases account for satellite-specific and receiver-specific hardware biases (e.g., Håkansson et al. (2017)). Combined satellite-and-receiver-specific biases, for example as observed by Hauschild et al. (2019), were not considered in the processing.

The system of equations is firstly solved in an iterative weighted batch least-squares adjustment. The ambiguities, initially treated as float-valued together with other real-valued parameters, are then decorrelated and fixed according to the methodology in Section 2. The experiments are limited to GPS and Galileo, either in a single- or dual-GNSS processing. To keep the setup as simple as possible, only observations with the RINEX 3 encoding C1C, C2W (GPS) and C1C/C1X, C5Q/C5X (Galileo) are used, along with their respective phase counterparts. The code and phase observations are processed at a 30-s sampling period. Satellite and receiver antenna calibrations are taken from "igsR3_2135.atx", i.e. the repro3 ANTEX file described in Villiger et al. (2020).

The station coordinates from a preliminary repro3 combined solution (IGSR03SNX) are introduced here as known, resulting in station-fixed solutions. This reduces the number of unknown parameters, allowing a more focused analysis of the impact of AR onto satellite products. In combination with the repro3 ANTEX file, it leads to products that are aligned to the IGSR3 reference frame. Any potential reference frame and antenna model differences affecting satellite orbit comparisons are taken into

Table 1
Estimated parameters per component and their a priori constraints (σ).

Component	Parametrization
Satellite orbits	Initial state, 7 ECOM2 parameters, stochastic pulse at midday ($\sigma = 0.1$ μm/s per axis)
Satellite/receiver clocks	Epoch-wise
Satellite/receiver code biases	Constant per day, signal (e.g., C1C), and constellation
Satellite phase biases	Constant per day, frequency, and constellation
Receiver phase biases	Constant per day, signal (e.g., L1C), and constellation
Phase ambiguities	Constant per continuous track and signal
Tropospheric zenith wet delay	Degree-1 spline with 2-hourly nodes per station ($\sigma = 5$ m)
Tropospheric gradient delays	Constant and trend per day and station in north and east directions ($\sigma = 5$ m)
Ionospheric influence	Slant total electron content per satellite-receiver line of sight and epoch

account in our analyses by means of a 7-parameter Helmert transformation. For example, IGS Final/CODE MGEX products used for evaluation are both aligned to the IGb14 reference frame and are based on different satellite antenna Z-offsets, which results in a difference in scale that is accounted for by the transformation parameters. The small global network adopted in the experiments is detailed in Section 3.2. In case any of the stations are unavailable on a specific day, they are replaced by nearby IGS stations to keep the network geometry as stable as possible.

State-of-the-art force and principal models have been applied in this processing, as described in Strasser et al. (2019). These are summarized in Table 2, where we refer to both dynamical accelerations for the satellite orbital motion and corrections to the GNSS code and phase observations. Since these two elements refer to inertial and non-inertial reference systems, the Earth orientation is introduced here as known based on the IERS EOP 14 C04 (IAU2000A) time series, along with an additional model covering the high-frequency effects (Desai and Sibois, 2016). An elevation-dependent stochastic model in the form $\sigma(el) = \sigma_z / \sin(el)$ is applied to define the a priori standard deviation of an observation based on its elevation angle "el", which is then used to weight the observations. Following repro3 configurations of GPS and Galileo, the standard deviation at zenith σ_z for raw code and phase observations is 22 cm and 1 mm, respectively.

3.1. Impact of ambiguity resolution with the network size

We start considering a global network of IGS stations, comprised of 60 well-distributed ground-based receivers, and a few sub-networks are selected starting from this largest one. The network and subsets are illustrated in Fig. 3, with a number of stations $M \in [10, 60]$.

For seven consecutive days (DOY 298–304 in 2019) we compute, on a daily basis, orbit and clock products considering GPS-only, Galileo-only and GPS+Galileo. Furthermore, in each configuration we compute both a float and a fixed solution. The latter is found based on an integer bootstrapping (IB) estimator and fixing for the most reliable subset (Verhagen et al., 2011) with a sufficient success rate, e.g. 99.9%. With IB, each ambiguity component is conditioned on the previous ones that are sequentially fixed by simply rounding. This conditioning introduces information that enhances the fixing success rate with respect to an Integer Rounding (IR) estimator where a component-wise rounding is performed. In this way, IB allows for a good computational efficiency with respect to integer search-

Table 2
The list of a priori models considered for the dynamical accelerations of satellite orbital motion and corrections to GNSS code and phase observations.

Dynamical accelerations	Model adopted	Reference
Earth's gravity field	GOCO06s	Kvas et al. (2021)
Astronomical tides	JPL DE432	Folkner et al. (2014)
Solid Earth tides	IERS 2010	Petit and Luzum (2010)
Ocean tides	FES2014b	Carrere et al. (2016)
Pole and ocean pole tides	IERS 2010	Petit and Luzum (2010)
Atmospheric tides	AOD1B RL06	Dobslaw et al. (2017)
General relativity	IERS 2010	Petit and Luzum (2010)
Solar radiation pressure	Box-wing	Rodriguez-Solano (2014)
Earth radiation pressure	Box-wing	Rodriguez-Solano (2009)
Antenna thrust	Narrow-beam	Steigenberger et al. (2018)
Observables corrections	**Model adopted**	**Reference**
Solid Earth tides	IERS 2010	Petit and Luzum (2010)
Ocean tides	FES2014b	Carrere et al. (2016)
Pole and ocean pole tides	IERS 2010	Petit and Luzum (2010)
Atmospheric tides	AOD1B RL06	Dobslaw et al. (2017)
Tropospheric delay	VMF3	Landskron and Böhm (2018)

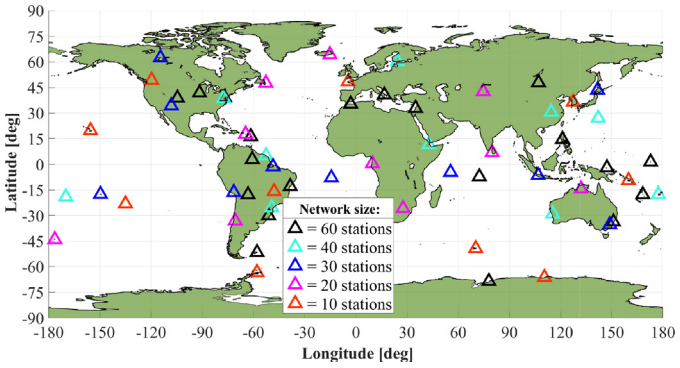

Fig. 3. Illustration of networks with different sizes between 10 and 60, with ground-based station receivers well distributed around the globe. Each smaller network is a subset of larger ones.

based processes, even if it remains sub-optimal and largely dependent upon the ambiguity parametrization.

The resulting satellite orbits are compared with reference orbits referring to IGS Final and CODE MGEX (Prange et al., 2020) products for GPS and Galileo, respectively. The overall 1D root mean square (RMS) of the orbit differences is therefore computed for all GNSS satellites involved in a certain scenario. The RMS values (in log-scale) are shown in Fig. 4, where we observe some relevant features. Each curve is related to a single daily solution (seven in total), while increasing the network size. All these global networks are subsets of larger ones, while we have considered some different sizes, e.g. $M = [10, 12, 14, 16, 18, 20, 25, 30, 40, 60]$.

In the float solutions (blue), the underlying observational model strength increases with a larger network and the overall RMS substantially decreases down to a 2–3 cm level. This is visible for both constellations and each configuration. In the fixed solutions (red), the overall RMS decreases quickly, but it reaches a plateau with global networks of around 25–30 stations. Adding more stations only leads to very small improvements in terms of orbit differences, as they ultimately become limited by the consistency between our estimates and the reference orbits in terms of force modeling and/or processing strategy (Section 3). Nonetheless, for $M = 25$, the satellite orbit differences (1D RMS) for GPS and Galileo fixed solutions are at 1–2 cm level, whereas the respective float solutions are at around 3–5 cm.

When focusing only on fixed solutions for small-size networks, i.e. $M \leqslant 20$, we note that IAR benefits seem somehow limited, probably due to a lower model strength of such small networks. In fact, a crucial condition for improving the accuracy of estimates (conditioned on the fixed carrier-phase ambiguities) is related to the successfulness of the IAR process. After all, given stochastic inputs to an integer estimator, also the outputs are expected to manifest a certain stochastic nature (Teunissen, 1998) and the least precise components might not be correctly fixed to their integer values. These wrong fixes might deteriorate our solution (e.g. jumps), while it is visible that for $M > 20$ we can (generally) already reach the 1–2 cm level in terms of orbit difference (1D RMS).

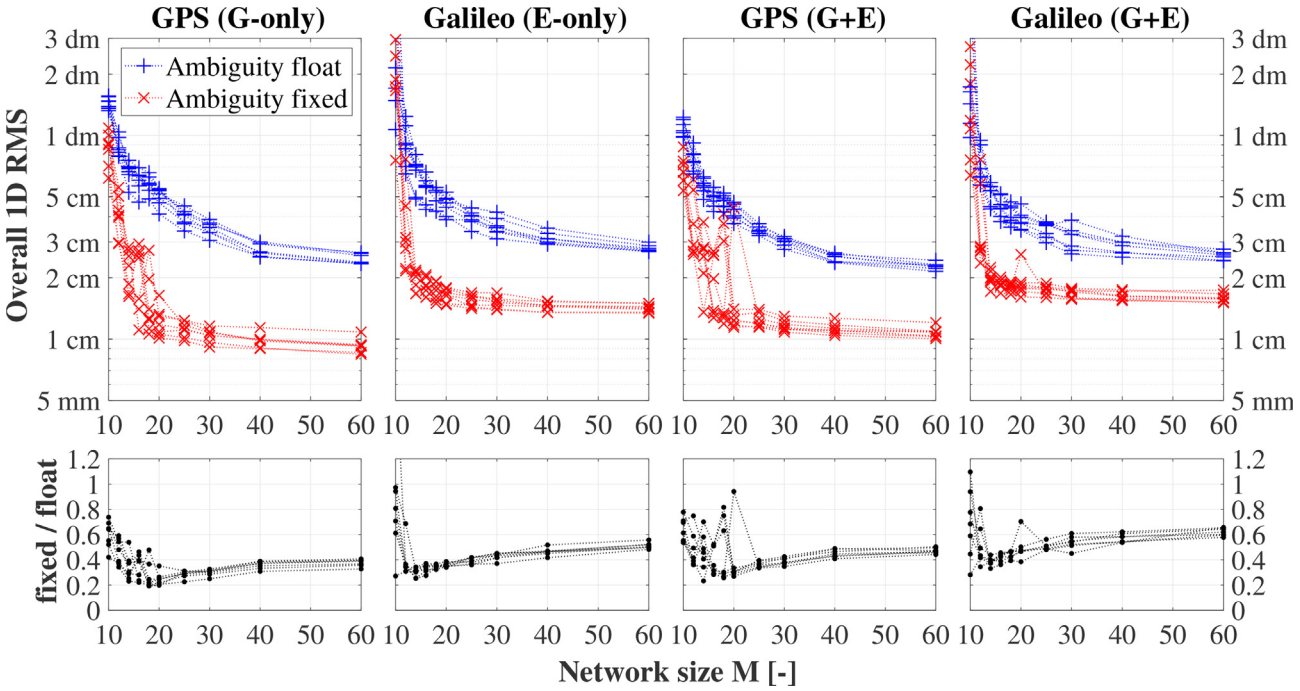

Fig. 4. The results for orbital (1D RMS) errors given for different GNSS configurations over 7 consecutive days. The notation (G+E) refers to results based on a GPS+Galileo combined processing, rather than G-only or E-only. Both ambiguity-float (in blue) and ambiguity-fixed (in red) solutions are shown, while the fixed/float ratio is given (in black) in the bottom plots. (For interpretation of the references to color in this figure legend, the reader is referred to the web version of this article.)

It is also interesting to compare the single- and dual-constellation processing. In fact, for the GPS+Galileo case, our fixed solutions (based on the same network) are showing slightly larger RMS values than for the respective GPS-only or Galileo-only scenario. The model inconsistencies between the two constellations might be compensated by real-valued ambiguities that are estimated (float solution), whereas they become more visible when applying the integer constraints (fixed solution). Moreover, in this dual-GNSS case, we are considering (integer-estimable) ambiguities mixed from both GPS and Galileo constellations, therefore processed as one full set. In this way, a between-constellation correlation is introduced. It seems interesting to further investigate such a GPS+Galileo scenario within small networks, e.g. looking at $M = 14$, whereas still thousands of ambiguities are involved.

3.2. Small-size network and configurations

We consider a small global network with 14 stations, and assuming a 5° elevation mask we obtain a visibility of 3 to 7 ground stations. For example, assuming a GPS satellite altitude, in Fig. 5 the number of ground-based stations visible at any point is illustrated by the depth-of-coverage (Blomenhofer et al., 2005). With Galileo satellites' higher altitude, and given the same elevation mask, station visibility is slightly increased. Hence, the depth-of-coverage is not exactly the same, nonetheless the patterns illustrated within Fig. 5 are found to be very similar.

In all our analyses, we consider a total of around 30 GPS and 24 Galileo satellites. This number can however change if certain satellites are not available on specific days. In general, for such a dual-frequency processing (and specified number of satellites/stations), we can find an ambiguity dimensionality of $n \approx 830$, 1290 and 2120 for Galileo-only, GPS-only and GPS+Galileo, respectively. Hence, with only 14 stations, we are already dealing with quite large dimensionalities and with more Galileo satellites having been deployed in 2020, this dimensionality might further increase.

In some very rare cases, some stations are replaced since they are not available on specific days in the 3-month period considered for our validation, here DOY 244 till 334 in 2019. In that case, the station is replaced by a different close-by IGS station. As a matter of example, SGOC is replaced by DGAR on DOY 263, and KRGG by PERT on DOY 322.

3.2.1. Block size selection for partitioning

The selection of suitable block sizes for the partitioning follows a balanced trade-off between the computational complexity, i.e. the efficiency aspect, and the reliability of fixed solutions, i.e. the robustness aspect. In this research work we consider a fixed block size q for all subsets, and in both VIB implementations we adopt $q = 200$, while in the Section 2.3 an example was given based on $q = 100$. The former value is found to be suitable for solving a GPS+Galileo HDAR problem (i.e. $n > 2000$) within a few tenths of a second in most of the experiments. Given that generally q is not a perfect divisor of n, we first process a (most precise) block with n_m components where $n_m = n - q \cdot \lfloor n/q \rfloor$ with $\lfloor \cdot \rfloor$ as the floor function. It follows that the other ambiguity blocks are given by $n_i = q$, for $i = m - 1, \ldots, 1$ and the number of blocks is simply found as $m = 1 + \lfloor n/q \rfloor$.

It should be remarked that for very small block sizes, e.g. $q \ll 100$, the integer search process is almost instantaneous, but we also have many more conditioning operations to perform. The latter might contribute to increase the overall computational effort since it involves additional matrix operations. The cost of such matrix operations, as well as for the integer search in each block, depends upon the computational capabilities and/or hardware of the platform in use, but is not numerically discussed in this work.

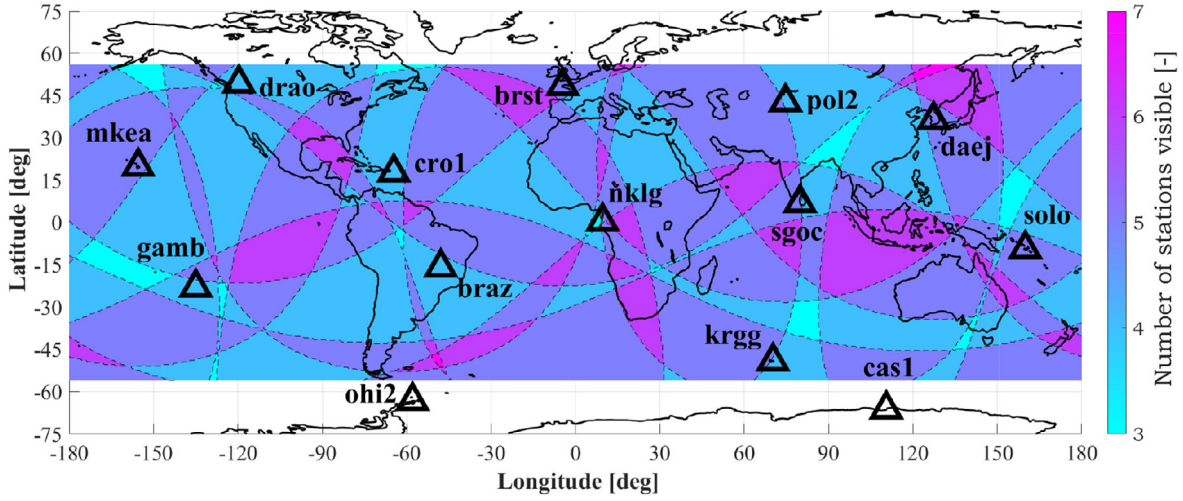

Fig. 5. The depth-of-coverage is given for GPS satellite altitude and 5° elevation mask in this small global network, which consists of 14 well-distributed ground-based stations.

Nonetheless, by using larger blocks we can obtain more reliable solutions, since closer to the optimality given by an ILS solution. Still, it is important to avoid ending up into computational bottlenecks due to the exponential growth of number of candidates spanned in the search tree for too large subsets.

4. ODTS results and comparison

In this section we focus on the small global network described in Section 3.2. Here, the different IAR strategies are compared and their beneficial impact onto satellite products is evaluated. When comparing the fixed results, we will refer to the integer bootstrapping estimator as 'IB', while 'CascAR' and 'TUG' are the two algorithms presented in Section 2.2 and Section 2.3, respectively. For the sake of convenience, we might refer to 'VIB' when results from CascAR and TUG are identical, for example in comparison with the (scalar) IB.

4.1. Results for Galileo-only

We start with the Galileo-only processing, where up to 850 ambiguities need to be fixed for each day. In this scenario, over the same testing week (DOY 298-304 in 2019) used in Fig. 4, we would be able to actually compute an ILS solution in less than a few seconds. The latter is possible due to the Z-transformation on ambiguity components, which improves the overall search time. Moreover, this decorrelation also makes quasi-optimal both the IB and VIB-based solutions, so leading here to the same integer solution as ILS. The latter is thus compared with respect to the float one.

The results are shown in Fig. 6, where the float and (ILS) fixed solutions are shown in black and magenta colors, respectively. For these seven days, the overall RMS of the entire constellation is computed epoch-wise. Looking at the radial component we see that a fixed solution allows RMS values below 3 cm for a large part of the day, whereas the float solution can exceed several centimeters. For the along-/cross-track components, large improvements are found and the overall RMS of fixed solutions are generally within a few centimeters. For what concerns the satellite clock component, smaller RMS errors are noted, but, as for the radial direction, the improvements are less pronounced.

These results are in agreement with the results of Li et al. (2019) and Laurichesse et al. (2013), since the ambiguity resolution in ODTS does not constrain much the radial direction due to its correlation with the clock error bias. Consequently, the largest improvements are generally found in the along-/cross-track error components. With respect to the float solution, the 1-week mean RMS value in the ILS solution is around 47% smaller for both radial and clock components. For what concerns the along- and cross-track components, the RMS value is 72% and 74% smaller, respectively.

For the sake of completeness, we might very briefly look at the error distribution, here based on all Galileo satellites over this 7-day analysis. In Fig. 7, the distribution is shown with four histograms (1 cm bins) for each component, while considering both a float and a fixed solution. It is visible that in the fixed case, most of the errors are bounded within 3 cm, although the largest improvements mainly concern along and cross components.

4.2. Results for GPS-only

When considering the GPS-only process, we deal with a higher dimensionality due to more satellites available at that time. Moreover, large computations for an ILS solution make this optimal solution unfeasible, possibly also due to the poorer stochastic model that affects the precision of float ambiguity estimates (Amiri-Simkooei et al., 2016). Several elements might concur in the uncertainty of observables, as investigated in (Hou et al., 2021), such as the robustness of different signals tracking scheme or the receiver model in use. Still, such features have not been further investigated in the scope of this work.

In order to enable fixed solutions within seconds (or less), we consider a quite reliable (and very efficient) IB

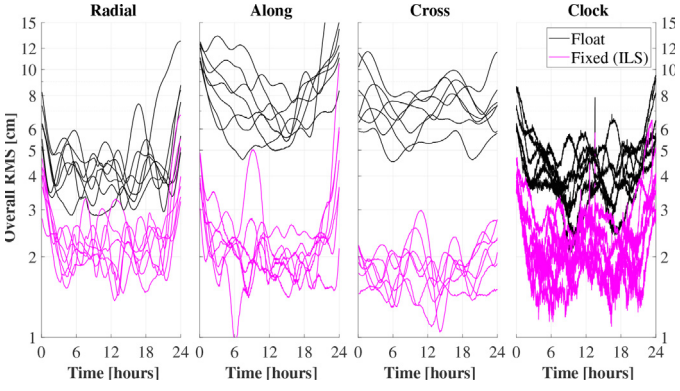

Fig. 6. The comparison for seven days of the epoch-wise RMS error over the entire constellation, divided into radial/along/cross orbital components and satellite clock error.

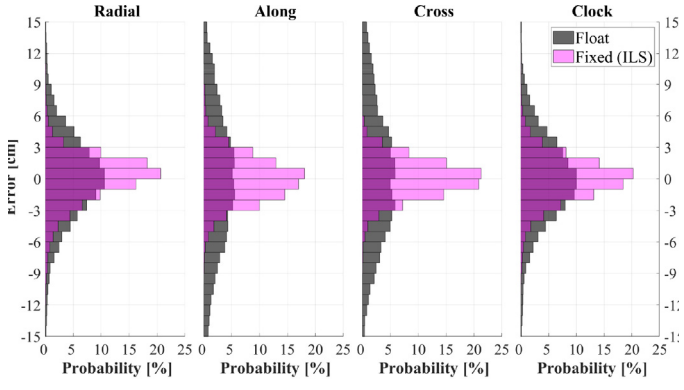

Fig. 7. The error distribution is shown for all Galileo satellites considering DOY 298 till 304 in 2019. The results are overlapped for a float and a (ILS) fixed solution, separating each component.

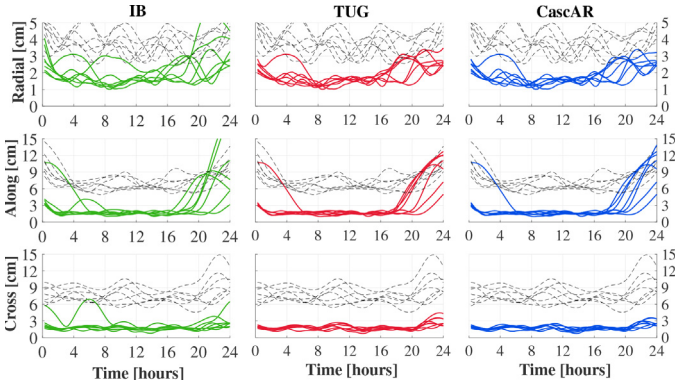

Fig. 8. The epoch-wise RMS of orbital components is shown for the fixed solutions with respect to float (dashed lines). A total of 7 days (DOY 298–304 in 2019) is used in this GPS-only processing.

solution, as well as the TUG and CascAR algorithms. All three solutions can largely benefit from the decorrelating Z-transformation that has been previously applied with LAMBDA. In this second scenario, the fixed solutions found with IB, TUG and CascAR are now different, and differ in terms of satellite orbit and clock estimates. Here, we focus our analysis mostly on the orbits, with Fig. 8 showing the epoch-wise overall RMS values per orbital component.

In almost all cases, both VIB-based solutions lead to same results, meanwhile the IB solution shows some larger errors in particular for DOY 300-302. In fact, RMS values might even largely exceed the ones for the respective float solution, as a possible consequence of wrong fixes. A different scale has been used for the radial component, where errors are within a few centimeters. It is interesting to observe, as expected, that the VIB-based results are generally equal to or better than the scalar IB ones (Teunissen et al., 2021).

A more detailed analysis shows that in most cases those larger errors are related to a one or two satellites, for example on DOY 302, but on some other days might be affecting more satellites, e.g. on DOY 300. This last case is shown in Fig. 9, where specific GPS satellites presenting large orbital errors have been highlighted in color (same in all solutions). The remaining ones are still shown in grey dashed lines, but are generally bounded within 5 cm.

A clear improvement is observed with respect to the float solution, nonetheless, the IB solution leads for many satellites to large orbital errors, up to 15 cm in the radial component and several decimeters for the along-track. In the VIB-based solutions we get large errors only in the case of a single satellite (PRN16), most likely due to a wrong fix. These issues of specific satellites cause the noticeably increasing RMS, particularly in the along-track component, towards the end of a day, as visible for most days in Fig. 8. In most cases, the underlying issue is short observation arcs caused by the cut-off at day boundaries which lead to ambiguities that are not well determined and can cause issues in ambiguity resolution. Due to the GPS ground-track repeat period of 1 sidereal day, this effect is very similar for the 7 days shown in Fig. 8. However, this is coincidental and a slowly changing observation geometry leads to this effect being less pronounced for other parts in the 91-day period.

Still, it is visible (as also for other testing days) that VIB solutions generally offer more reliable fixes without much impacting the computational effort, later discussed in Section 4.4. For instance, HDAR solutions of such a dimensionality (n≈1300) can be often found within hundredths of a second for standard desktop processors, e.g. Intel i7-4790 @3.6 GHz. As a matter of example, in Fig. 10 we show the RMS values (over these 24 h on DOY 300) for all GPS satellites based on the four solutions previously discussed. The CascAR and TUG solutions are identical on this day, as is the case on almost all days of this scenario. With respect to the float solution, the R/A/C components are improved here by around 31/42/71% and 52/67/77% for the IB and both VIB solutions, respectively. As already seen for the Galileo-only ODTS results, larger benefits of fixed solutions are mostly observed in the along-/cross-track components.

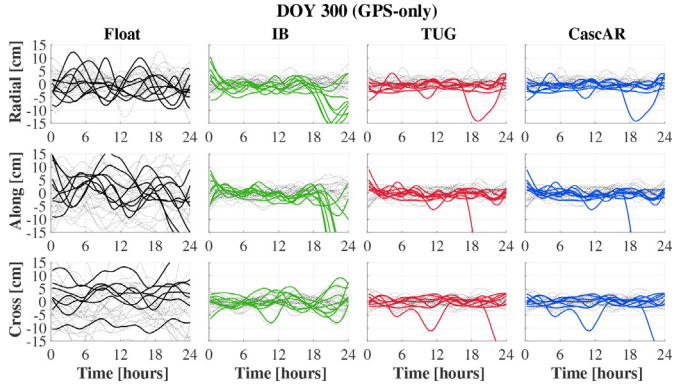

Fig. 9. The orbital errors over 24 h (DOY 300) for different solutions, considering GPS-only and highlighting (with colors) certain satellites where fixed-solution errors are quite large. (For interpretation of the references to color in this figure legend, the reader is referred to the web version of this article.)

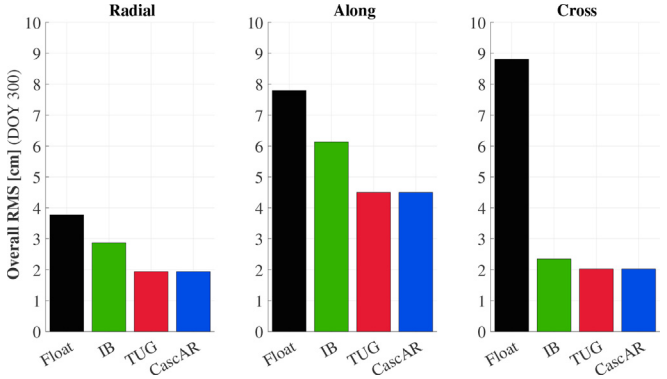

Fig. 10. The overall RMS error is shown relative to a 24-h period, i.e. DOY 300 in 2019. For each orbital component, we consider the float (black) and three fixed solutions.

4.3. Results for GPS+Galileo

At this point we can focus our investigation on the GPS +Galileo processing scenario. This is also the most interesting one, due to a larger ambiguity dimensionality involved, where in general for our small network we always have $n > 2000$. For a more extensive analysis of this HDAR problem, we consider a 3-month period in 2019, starting from DOY 244 till 334, both days included. We examine the solutions for these 91 days, so processing GPS+Galileo on a daily basis as described in Section 3.

Firstly, we start considering the RMS errors over all days while referring to each satellite for GPS and Galileo, and each orbital component. These RMS values are then divided with the ones relative to a float solution (dashed line), and ratios are provided, as percentages, in Fig. 11. Smaller % values imply larger improvements with respect to the float solution, which is often the case. For GPS satellites, the mean improvement in terms of R/A/C orbital components is approximatively 28/44/56% and 33/50/63% for the IB and the VIB-based solutions, respectively. For Galileo satellites, this is approximatively 30/56/62% for the IB, while 32/60/64% again for both TUG and CascAR solutions. These two VIB solutions show a high consistency in the results, but not always the exact same solutions.

At this point we can consider in Fig. 12 the results in terms of overall orbital errors (1D RMS) for GPS (left plot) and Galileo (right plot). For each day we compute values over all satellites (and components) of each constellation. By comparing the fixed solutions for Galileo, we see that they are usually quite similar, with the exception of specific days where the (scalar) IB solution shows much larger errors with respect to TUG or CascAR. This is for instance visible on DOY 268 where the 1D RMS value exceeds 12 cm. In these Galileo results, a slight discrepancy is also visible for the TUG and CascAR solutions, specifically on DOY 294, which is discussed in more details later in Section 4.4.

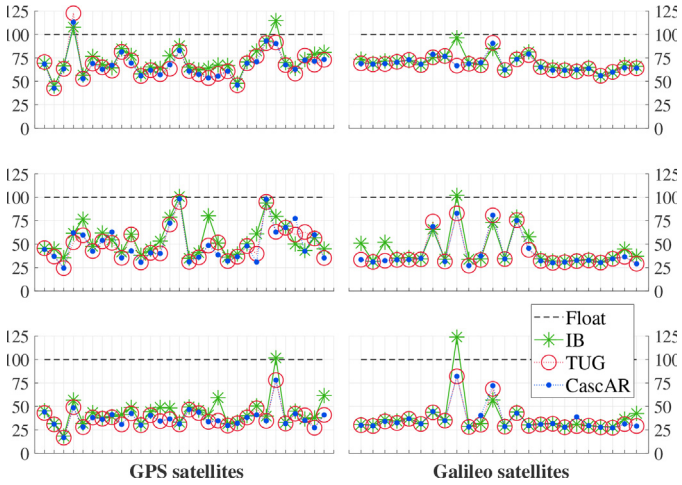

Fig. 11. The results for all GPS and Galileo satellites are given in terms of RMS ratio w.r.t. float solution for each orbital component over the 3-month period considered (DOY 244-334 in 2019).

When looking at the GPS results, similarly to what was seen in Section 4.2, we observe several 1D RMS differences, and on several days we have high values for the IB. This is again most likely due to wrong fixes, which deteriorates the performance of the ODTS process in this small global network estimation. With respect to the Galileo results, float values are generally found at around 5 to 7 cm, whereas we have observed some much higher peaks in Galileo during the first four weeks, i.e. in September 2019. Nevertheless, this particular behavior has not been further investigated in the context of this research work.

Before proceeding with the validation of these GPS +Galileo results, we might firstly consider a small comparison between the two VIB methods.

4.4. Comparison between TUG and CascAR solutions

The high consistency shown between VIB-based solutions is mostly due to the similarity of the two algorithms, although in the TUG "blocked search" approach additional checks are performed on the integer solution by looking at overlapping blocks (see Section 2.3). If the solutions are always consistent in each overlap, then both TUG and CascAR are basically equivalent, i.e. return the same integer solution. This is the case for most of the days tested here, however, not always. By a detailed comparison in Fig. 12, only in a few occasions the two VIB-based results are quite different. For DOY 294 we clearly see CascAR being suboptimal to both IB and TUG. In Fig. 13, we present the orbital errors (as 3D scalar displacement) for all 54 satellites over the 24 h on DOY 294. It is visible that in the CascAR solution, some wrong fixes occur and results are largely affected, with errors exceeding some decimeters. It should be mentioned that such large errors are not only affecting Galileo, but GPS as well, and in general only limited to very specific days.

At this point we might wonder whether such robustness of the TUG algorithm comes at a higher computational cost, thence on a much lower efficiency. As mentioned, the VIB-based approaches allow for high flexibility in the design of most effective algorithms, but this also depends on the specific application, the considered scenarios and/or available computational capabilities. Hence, the daily computational time is very briefly compared for the different IAR methods considered in this numerical experiment.

The IB solution is generally computed in a few milliseconds and it is only dependent upon the ambiguity problem dimensionality, which was quite constant over this 3-month period. For instance, in the GPS+Galileo processing we have always between 2050 and 2250 ambiguity components. In Fig. 14, we show the computation times for the two VIB-based solutions, based on an average over 100 runs. It is visible that both VIB-based solutions are computationally more expensive than IB, but they seem to provide a more reliable solution as shown in the previous section, and further validated in Section 5. Still, for most of the cases, a HDAR solution (i.e. $n > 2000$) can be found

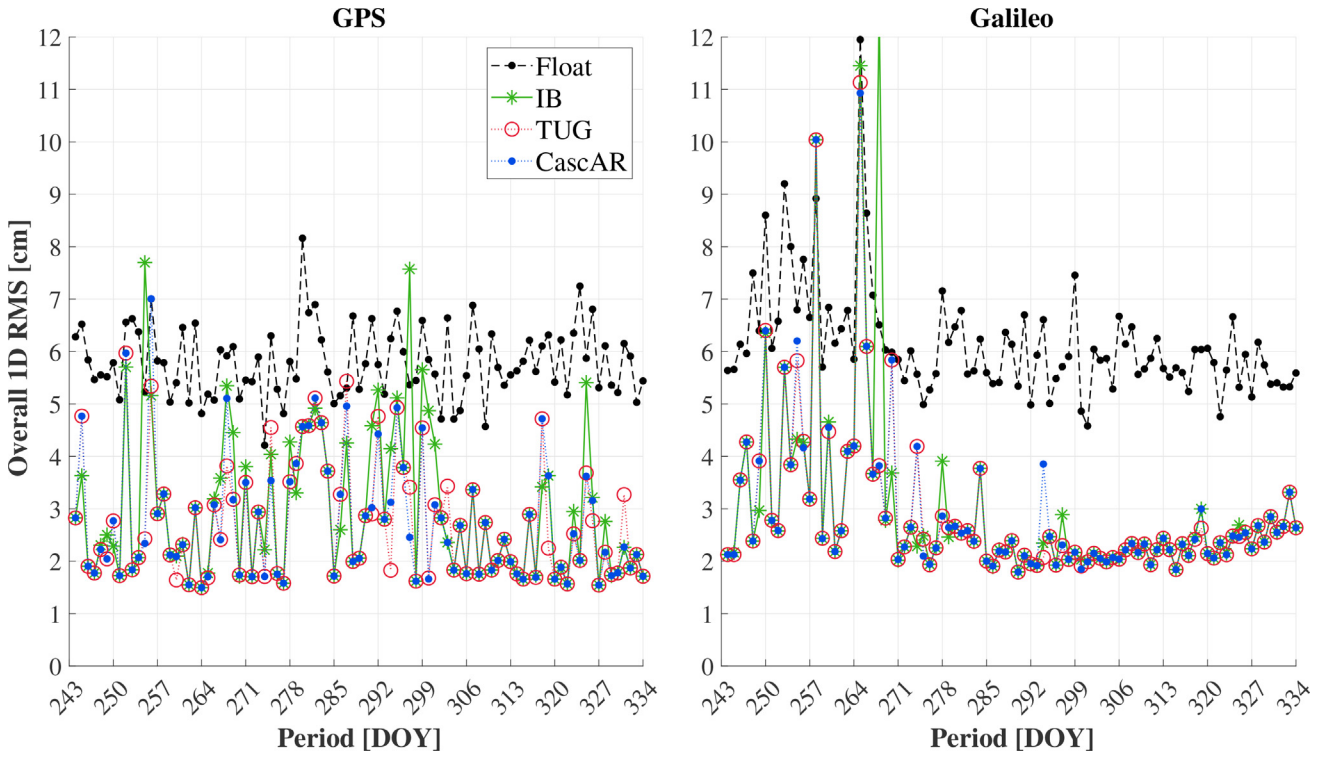

Fig. 12. GPS+Galileo results in daily 1D RMS values over each constellation. The float solution is shown, along with three fixed ones: IB, TUG and CascAR.

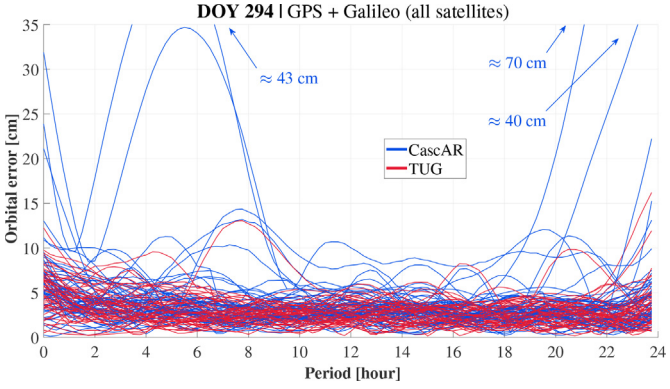

Fig. 13. A detailed example for DOY 294 (in 2019) concerning the epoch-wise orbital errors of all satellites processed (different curves) with TUG and CascAR ambiguity resolution methods.

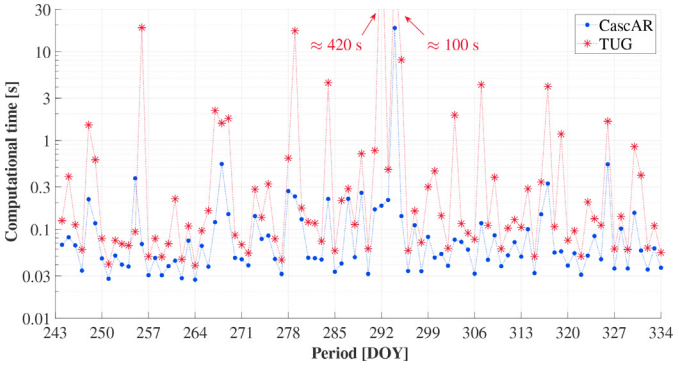

Fig. 14. The computational time (log-scale), averaged over 100 runs, is given for the TUG and the CascAR algorithms with respect to the GPS +Galileo HDAR problem ($n > 2000$).

within a few tenths of a second, e.g. here based on the Intel Core i7-4790 @3.6 GHz central processor.

For what concerns the TUG algorithm, the computational time is indeed higher due to the overlapping strategy mentioned in Section 2.3. In only one case, on DOY 255, the search time is larger for the CascAR approach, while it only exceeds 0.6 s once, i.e. ~20 s on DOY 294. The 91-day averaged ratio of CascAR over TUG computational time is 47.8%, therefore being twice as efficient as the TUG algorithm. The much-increased search times observed on some days for the TUG method is caused by the expansion to larger block sizes in case the overlapping of fixed ambiguity components does not match. In fact, in many occasions we see that for the TUG approach it takes more than 0.6 s to compute an integer solution to the HDAR problem.

Finally, we should not forget that these examples of VIB algorithms are only two possible implementations, leaving further more advanced strategies still to be investigated. A few suggestions will be given in Section 5.2. We can now continue to focus on a validation of results for the GPS +Galileo scenario.

5. Validation and discussion

We can now present a further analysis of the results, where a different metric is adopted. In fact, as mentioned,

the adoption of external products as 'ground truth' for the evaluation of orbit and clock errors has some limitations in terms of consistency. Given that we have processed network data on a daily basis, we might instead consider the orbital discontinuity at midnights. This evaluation strategy is independent from external sources and quantifies jumps in satellite orbits between consecutive days.

5.1. Analysis of orbital discontinuity at midnight

The GPS+Galileo scenario is considered, and for each satellite we compute the 1D RMS of orbital discontinuities at the midnight between two consecutive days. For the float solution we have always larger discontinuities, almost always exceeding 10 cm and it is therefore not illustrated here. Furthermore, TUG and CascAR solutions are matching basically in most of the results, except for 1–2 days. This difference has been already discussed in Section 4.4, so for this analysis we focus on IB versus VIB, the latter referring to the TUG solution. These results (over the 3-month period) are provided in Fig. 15 based on a color scale between 0 and 10 cm, while separating the satellite groups for each constellation.

In the IB case, we see that many days present much larger values with respect to the vectorial counterpart. The VIB solution is sometimes exceeding the dm-level only for a few satellites, i.e. E14/E18 for Galileo and G05/G16/G26 for GPS. In the former case it should be noted that those two satellites are the ones placed into slightly elliptical orbits, making it more challenging to properly model their orbit and attitude.

The most notable differences between IB and VIB clearly fully affect either one or both GNSS constellations, so we can examine the range of discontinuity values for both constellations. For each midnight epoch we compute a box plot over each system and results are shown in Fig. 16 for the three methods: the float solution, along with the fixed IB and VIB ones. A box plot visualizes the median value as a red line within a blue box that defines the interquartile range, i.e. the difference between 75th and 25th percentiles. The full range is given by grey whiskers, excluding outliers that are marked as red dots.

Many days show only small improvements when comparing IB to VIB, but on some days the discontinuities are much smaller in case of VIB-fixed solutions. However, improvements with respect to the float case are always evident. It is interesting to observe that for the (scalar) IB estimator we have, on specific days, errors exceeding the float ones. Once again, a wrong fixing can lead to an inconsistent satellite orbit, and this can impact the discontinuity values at the boundary/ies of that particular day. In this circumstance, many satellites might be affected and fixed results are visibly worse than the float solution.

At this point, for the sake of completeness, we define an overall empirical cumulative distribution of these orbit midnight discontinuity errors for each solution. Also in this case, both VIB-based solutions are represented by a single curve since no (visible) differences were found. In Fig. 17 we see that in terms of orbit midnight discontinuity errors,

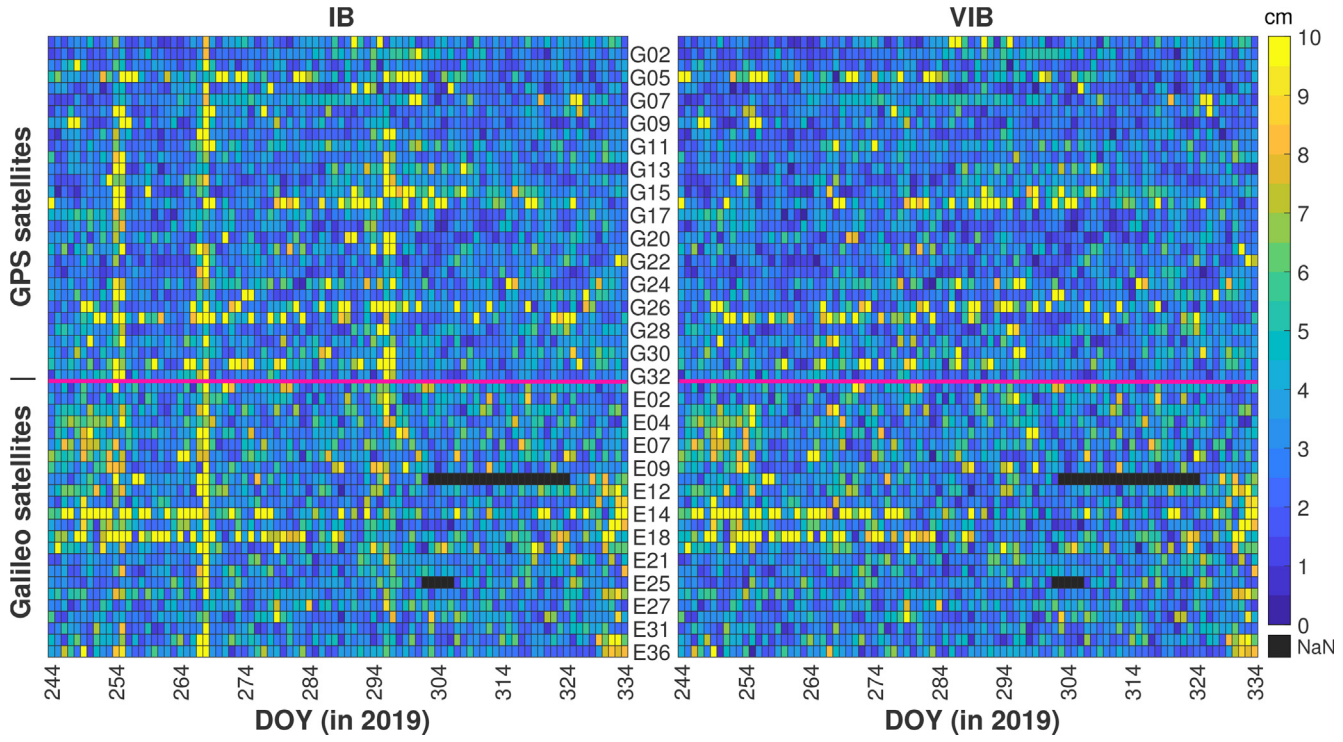

Fig. 15. The satellite orbit discontinuity errors at midnight are shown for GPS+Galileo processing over a 3-month period in 2019. Both IB and VIB solutions are considered, as described in the text.

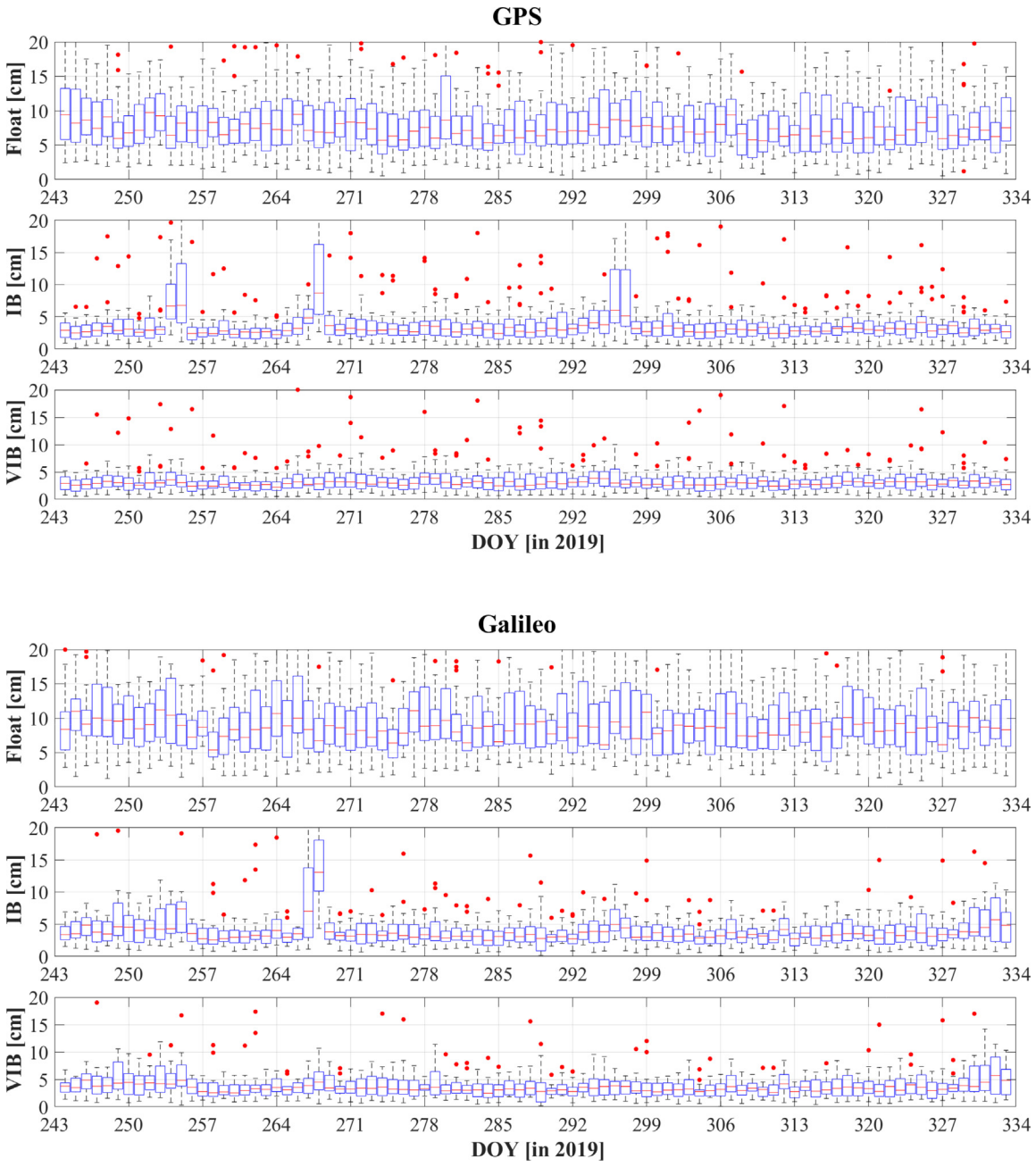

Fig. 16. The box plot results for midnight discontinuities of GPS and Galileo considering three methods based on a float solution, then a scalar (IB) and a vectorial (VIB) integer bootstrapping.

over the 91 days, the float solution has quite large errors, and in 50% of the cases those values exceed 8 cm. For the fixed solutions we have around 3 cm, with a negligible difference between the two methods. At 95% probability, float-solution errors are around 18.3 cm, roughly twice the respective value of the fixed solutions. This also confirms how substantial improvements can be achieved by robust (and ideally efficient) ambiguity resolution schemes in the estimation of satellite orbits and clocks, even when using a small global network.

We need to remark that such a good result is possible also thanks to the LAMBDA decorrelation of ambiguities. In fact, this can substantially improve the optimality of integer bootstrapping approaches. Still, the VIB solutions further improve the results with respect to the scalar IB, thus reducing the discontinuity errors from 10 to 8 cm (at 95% probability). As mentioned in Section 4.4, these more reliable solutions are possible without too much compromising the computational efficiency of the IAR process. Lastly, it should be remarked that enhancements at the decorrelation step might further benefit the here presented VIB formulations, where an example of comparison among different "reduction" methods can be found in Jazaeri et al. (2014).

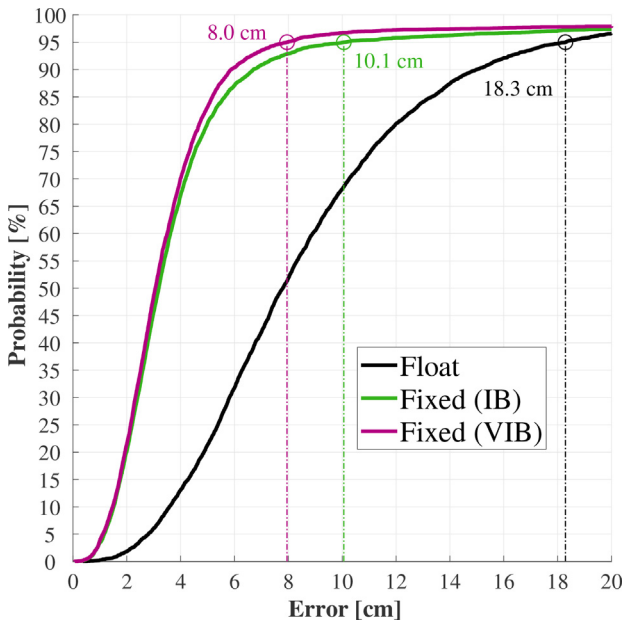

Fig. 17. Empirical cumulative distribution for midnight discontinuity errors relative to the different solutions and all satellites processed over the 3-month period (DOY 244–334 in 2019). The error values at 95% probability are marked with circles.

5.2. Limitations and further possibilities

When adopting VIB, it is important not to generalize properties of a certain estimator to the entire ambiguity set. For example, the optimality of ILS within each block does not hold for the full set where VIB solutions are indeed suboptimal with respect to an ILS solution over the full n-dimensional set. The use of larger ambiguity blocks can lead to higher robustness performance, but sometimes at a very high cost for the efficiency. With the VIB approaches, here focused on a small global network, the daily fixed solutions can still be computed in less than a second and generally lead to smaller errors. On some days, these errors might exceed a few decimeters when making use of the (still convenient) integer bootstrapping estimator.

The VIB formulation shall not be restricted to the use (in each subset) of I-estimators, e.g. ILS, but it can benefit from more advanced schemes (Teunissen et al., 2021). Hence, by the use of a vectorial formulation, it is possible to combine different types and/or classes of estimators in this vectorial approach. As mentioned, a proper selection of the partitioning strategy can depend upon computational resources available, along with applications and latencies that users would like to be addressed by the IAR process.

For instance, adoption of integer validation tests (i.e. a data-driven approach) is possible and it might further prevent the wrong fixing of some ambiguity subsets. In addition to that, more efficient estimators, for example rounding or bootstrapping, might be used only in the more precise ambiguity subsets, while adopting ILS in the remaining ones. Another notable example of VIB-like strategies is given by the Sequential Best Integer Equivariant (SBIE) approach, described in Brack et al. (2013), which enables a more efficient adoption of BIE-related solutions. Still, in their work, this was limited to a scalar case, therefore not taking full advantage from the vectorial formulation analyzed in this research contribution.

6. Conclusions

The high complexity involved in the search for an optimal integer least-squares solution to high-dimensional ambiguity resolution (HDAR) problems is still a challenge. In order to find a trade-off between robustness and efficiency of a certain IAR process, in this work we present two implementations of a vectorial integer bootstrapping (VIB) estimator. Based on the VIB principle, introduced in Teunissen et al., 2021, it is possible to design more flexible IAR algorithms. This allows finding an effective solution to a given HDAR problem, thus balancing available computational resources and reliability of the fixed solutions.

The two algorithms are CascAR, as a straightforward implementation of VIB, and the "blocked search" method developed at Graz University of Technology. In both cases, we take advantage of the same initial triangular decomposition, along with LAMBDA Z-transformation to decorrelate the ambiguity components. These two VIB-based solutions are therefore compared with respect to their scalar counterpart, i.e. Integer Bootstrapping (IB) estimator, and investigated in the context of Orbit Determination and Time Synchronization (ODTS). This is performed based on TUG's open-source software GROOPS.

Firstly, we consider for different network sizes, between 10 and 60 stations, the 1D RMS orbital errors relative to GPS-only, Galileo-only and GPS+Galileo scenarios. In all cases, we adopt a 24-h batch processing and 30-s sampling period for dual-frequency code and phase observations. The float and IB fixed solutions are considered, the latter showing a plateau at 1–2 cm, reached with 25 or more well-distributed stations. When looking at smaller networks the improvements over the float solutions are significant, but in several occasions wrong fixes might lead to quite large orbital errors. Hence, we focus our investigation on a small global network, i.e. 14 stations, where the three IAR strategies are evaluated and compared.

In the Galileo-only case, all fixed solutions seem to be optimal over the entire set and lead to large improvements over the float results, both evaluated with respect to the CODE MGEX products. On several days, the mean RMS (radial and clock) for a fixed solution can be around 50% smaller than the float one, and more than 70% for both along-and cross-track error components. These last two are in fact generally more affected by IAR, in agreement with literature. In the GPS-only case, with respect to IGS Final products, more visible differences are found among fixed solutions, where orbital errors in the radial/along/cross component can be improved (e.g. on DOY 300) by 31/42/71% and 52/67/77% for IB and VIB solutions, respectively.

The most interesting scenario considered is the GPS +Galileo processing, where more than 2000 ambiguities are fixed per day. This HDAR problem is not trivial, especially when looking for a computationally cheap and reliable fixed solution. Both GPS and Galileo are processed together, so an inter-system correlation of carrier-phase ambiguities might be introduced. The scenario is numerically assessed on a daily basis over a 3-month period (DOY 244 till DOY 334 in 2019), and then analyzed separately for each constellation. In some days, the IB solution shows much larger orbital errors (in terms of RMS over each single constellation), which can exceed several centimeters.

The validation of the GPS+Galileo results is performed by an intrinsic quality check, thus not relying on external orbital information. We look at the orbit discontinuity errors at midnights over the 3-month period. For multiple days, the discontinuities based on an IB solution are quite large, whereas VIB-based methods provide better results. The two different VIB approaches present quite similar performances over all tests, as expected; nonetheless the TUG solution further improves the results on a few occasions. This comes at a higher computational cost, shown for each day over the testing period. Still, in most of the cases, this HDAR problem can be robustly solved within fractions of a second, while providing substantial benefit to the ODTS estimates. By means of VIB fixed solutions, with a global network of 14 stations, it is possible to compute orbits within a few centimeters error.

The vectorial formulation shows to be a suitable candidate, due to its flexibility, in the design of more effective IAR algorithms, in particular for HDAR problems. It enables a trade-off between efficiency and robustness, based on a very easy-to-implement strategy that has been extensively described in this work. Although referring here to the case of small global network estimation, its applicability extends over any mixed-integer GNSS model, and shall not be restricted to the network case. Additional works, also involving other classes of estimators or different strategies, shall be conducted to further exploit the VIB theory.

Data Availability

The multi-GNSS observation data, along with IGS Final and CODE MGEX products, are available at the IGS global data centers (https://www.igs.org/data-products-overview). The Earth Orientation Parameters (EOPs) are provided by the International Earth Rotation and Reference Systems Service (IERS, https://www.iers.org). The precise coordinates for IGS tracking stations are made available by the National Institute of Geographic and Forest Information (IGN, ftp://igs-rf.ign.fr).

Declaration of Competing Interest

The authors declare that they have no known competing financial interests or personal relationships that could have appeared to influence the work reported in this paper.

Acknowledgments

This work has been initiated in the framework of TREASURE, which has received funding from the European Union's Horizon 2020 research and innovation programme under the Marie Skłodowska-Curie Grant Agreement No. 722023. Parts of the presented work were funded by the Austrian Research Promotion Agency (FFG) in the frame of the Austrian Space Applications Programme (ASAP) Phase 16 (Project No. 878886). The author LM wants to thank Deimos Engenharia, where has been working during this research conceptualization, along with Dr. Sandra Verhagen and Prof.Dr. Peter Teunissen for their insightful remarks on this research contribution. The authors acknowledge the institutions associated with the IGS and MGEX, which provide GPS and Galileo observation data, along with precise satellite orbit and clock products.

Appendix A

The implementation of a generic VIB estimator can benefit from a conformed partitioning of the triangular decomposition for the ambiguity vc-matrix, i.e. $\tilde{Q} \simeq \tilde{L}^T \tilde{D} \tilde{L}$. Based on Eq. (4), we can consider $\tilde{L} \in \mathbb{R}^{n \times n}$ (lower unitriangular) and $\tilde{D} \in \mathbb{R}^{n \times n}$ (diagonal), such as

$$\tilde{L} = \begin{bmatrix} \tilde{L}_{11} & 0 \\ \tilde{L}_{Q} & \tilde{L}_{22} \end{bmatrix}, \quad \tilde{D} = \begin{bmatrix} \tilde{D}_1 & 0 \\ 0 & \tilde{D}_2 \end{bmatrix} \tag{A.1}$$

and for $k = 1, 2$, we have that $\tilde{L}_{kk} \in \mathbb{R}^{n_k \times n_k}$ is lower unitriangular, $\tilde{D}_{kk} \in \mathbb{R}^{n_k \times n_k}$ is diagonal, while $\tilde{L}_Q \in \mathbb{R}^{n_2 \times n_1}$ is a rectangular block matrix. The latter one represents the correlation between the two subsets, therefore involved in the conditioning, i.e. here $\{2\} \rightarrow \{1\}$.

It is straightforward to prove that each block of the vc-matrix $\tilde{Q}$ is retrieved from

$$\tilde{Q} \overset{\text{def}}{=} \begin{bmatrix} \tilde{Q}_{11} & \tilde{Q}_{12} \\ \tilde{Q}_{21} & \tilde{Q}_{22} \end{bmatrix} = \begin{bmatrix} \tilde{L}_{11}^T \tilde{D}_1 \tilde{L}_{11} + \tilde{L}_Q^T \tilde{D}_2 \tilde{L}_Q & \tilde{L}_Q^T \tilde{D}_2 \tilde{L}_{22} \\ \tilde{L}_{22}^T \tilde{D}_2 \tilde{L}_Q & \tilde{L}_{22}^T \tilde{D}_2 \tilde{L}_{22} \end{bmatrix} \tag{A.2}$$

while the first ambiguity block, conditioned on the second one, is described by $\tilde{Q}_{11|22}$ as follows

$$\begin{aligned} \tilde{Q}_{11|22} &= \tilde{Q}_{11} - \tilde{Q}_{12} \tilde{Q}_{22}^{-1} \tilde{Q}_{21} \\ &= \tilde{Q}_{11} - (\tilde{L}_Q^T \tilde{D}_2 \tilde{L}_{22})(\tilde{L}_{22}^{-1} \tilde{D}_2^{-1} \tilde{L}_{22}^{-T})(\tilde{L}_{22}^T \tilde{D}_2 \tilde{L}_Q) \\ &= \tilde{L}_{11}^T \tilde{D}_1 \tilde{L}_{11} \end{aligned} \tag{A.3}$$

that represents its unique $L^T DL$-decomposition due to the form of matrices $\tilde{L}_{11}$ and $\tilde{D}_1$. These mathematical relationships also enable a straightforward computation of the conditioning for the float ambiguity subset $\{1\}$, given $\hat{a}_k \in \mathbb{R}^{n_k}$ for $k = 1, 2$. Hence, we can write

$$\begin{aligned}\hat{a}_{1|2} &= \hat{a}_1 - \tilde{Q}_{12}\tilde{Q}_{22}^{-1}\cdot(\hat{a}_2 - \check{a}_2)\\ &= \hat{a}_1 - (\tilde{L}_Q^T\tilde{D}_2\tilde{L}_{22})(\tilde{L}_{22}^{-1}\tilde{D}_2^{-1}\tilde{L}_{22}^{-T})\cdot(\hat{a}_2 - \check{a}_2)\\ &= \hat{a}_1 - \tilde{L}_Q^T\tilde{L}_{22}^{-T}\cdot(\hat{a}_2 - \check{a}_2)\end{aligned} \tag{A.4}$$

with all matrix blocks already available from Eq. (A.1). In this case, for example, we have that $\check{a}_2 = \mathcal{I}_2(\hat{a}_2)$, where $\mathcal{I}_2$ can be any integer mapping function taken from the class of

- **I-estimators** (Teunissen, 1999), which always return $\check{a}_2 \in \mathbb{Z}^{n_2}$ (integer-valued);
- **IE-estimators** (Teunissen, 2002), which always return $\check{a}_2 \in \mathbb{R}^{n_2}$ (real-valued);
- **IA-estimators** (Teunissen, 2003a), which either return an integer- or a real-valued ambiguity vector, depending upon the result of the integer validation test.

With Eq. (A.3), we observe that the metric for the block $\{1\}$, being conditioned on $\{2\}$, is already 'extracted' from the same initial triangular decomposition. Furthermore, a selection of n_k values was arbitrary, and by setting $\tilde{L} \equiv \tilde{L}_{11}, \tilde{D} \equiv \tilde{D}_1$, we can further partition the sub-problem, thus equivalently obtaining an arbitrary number $m \in [1, n]$ of subsets. Each one can have an arbitrary dimensionality, as long as their sum is equal to n.

We should remark that such a partitioning strategy holds also if looking at a reversed conditioning, therefore $\{1\} \rightarrow \{2\} \rightarrow \ldots \rightarrow \{m\}$. In this case we would need to consider a different decomposition, e.g. see De Jonge and Tiberius (1996), so having $\tilde{Q} = \tilde{L}\tilde{D}\tilde{L}^T$, where $\tilde{L}$ and $\tilde{D}$ are once again a lower unitriangular and a diagonal matrix, respectively.

References

Amiri-Simkooei, A.R., Jazaeri, S., Zangeneh-Nejad, F., Asgari, J., 2016. Role of stochastic model on GPS integer ambiguity resolution success rate. GPS Solut. 20 (1), 51–61. https://doi.org/10.1007/s10291-015-0445-5.

Arnold, D., Meindl, M., Beutler, G., Dach, R., Schaer, S., Lutz, S., Prange, L., Sośnica, K., Mervart, L., Jäggi, A., 2015. CODE's new solar radiation pressure model for GNSS orbit determination. J. Geodesy 89 (8), 775–791. https://doi.org/10.1007/s00190-015-0814-4.

Blewitt, G., 1989. Carrier phase ambiguity resolution for the Global Positioning System applied to geodetic baselines up to 2000 km. J. Geophys. Res.: Solid Earth 94 (B8), 10187–10203. https://doi.org/10.1029/JB094iB08p10187.

Blomenhofer, H., Ehret, W., Blomenhofer, E., 2005. Investigation of the GNSS/Galileo integrity performance for safety of life applications. In: Proceedings of European GNSS.

Brack, A., 2019. Partial carrier-phase integer ambiguity resolution for high accuracy GNSS positioning. Ph.D. thesis Technische Universität München.

Brack, A., Henkel, P., Gunther, C., 2013. Sequential best integer-equivariant estimation for geodetic network solutions. In: Proceedings of the 2013 International Technical Meeting of The Institute of Navigation, pp. 310–317.

Carrere, L., Lyard, F., Cancet, M., Guillot, A., Picot, N., et al., 2016. FES 2014, a new tidal model–validation results and perspectives for improvements. In: In Proceedings of the ESA living planet symposium, pp. 9–13.

Chen, H., Jiang, W., Ge, M., Wickert, J., Schuh, H., 2014. An enhanced strategy for GNSS data processing of massive networks. J. Geodesy 88 (9), 857–867. https://doi.org/10.1007/s00190-014-0727-7.

Cocard, M., Geiger, A., 1992. Systematic search for all possible widelanes. In: Proceedings of the 6th International Geodetic Symposium on Satellite Positioning, pp. 312–318.

De Jonge, P., Tiberius, C., 1996. The LAMBDA method for integer ambiguity estimation: implementation aspects. Publications of the Delft Computing Centre, LGR-Series 12 (12), 1–47.

Desai, S.D., Sibois, A.E., 2016. Evaluating predicted diurnal and semidiurnal tidal variations in polar motion with GPS-based observations. J. Geophys. Res.: Solid Earth 121 (7), 5237–5256. https://doi.org/10.1002/2016JB013125.

Dobslaw, H., Bergmann-Wolf, I., Dill, R., Poropat, L., Thomas, M., Dahle, C., Esselborn, S., König, R., Flechtner, F., 2017. A new high-resolution model of non-tidal atmosphere and ocean mass variability for de-aliasing of satellite gravity observations: AOD1B RL06. Geophys. J. Int. 211 (1), 263–269. https://doi.org/10.1093/gji/ggx302.

Folkner, W.M., Williams, J.G., Boggs, D.H., Park, R.S., Kuchynka, P., 2014. The planetary and lunar ephemerides DE430 and DE431. Interplanetary Network Progress Report 196 (1).

Ge, M., Gendt, G., Dick, G., Zhang, F., Rothacher, M., 2006. A new data processing strategy for huge GNSS global networks. J. Geodesy 80 (4), 199–203. https://doi.org/10.1007/s00190-006-0044-x.

Hauschild, A., Steigenberger, P., Montenbruck, O., 2019. Inter-receiver GNSS pseudorange biases and their effect on clock and DCB estimation. In: Proceedings of the 32nd International Technical Meeting of the Satellite Division of The Institute of Navigation (ION GNSS+ 2019), pp. 3675–3685. doi: 10.33012/2019.16975.

Håkansson, M., Jensen, A.B.O., Horemuz, M., Hedling, G., 2017. Review of code and phase biases in multi-GNSS positioning. GPS Solut. 21 (3), 849–860. https://doi.org/10.1007/s10291-016-0572-7.

Hou, P., Zhang, B., Yuan, Y., 2021. Analysis of the stochastic characteristics of gps/bds/galileo multi-frequency observables with different types of receivers. J. Spatial Sci. 66 (1), 49–73. https://doi.org/10.1080/14498596.2019.1578274.

Jazaeri, S., Amiri-Simkooei, A., Sharifi, M., 2012. Fast integer least-squares estimation for GNSS high-dimensional ambiguity resolution using lattice theory. J. Geodesy 86 (2), 123–136. https://doi.org/10.1007/s00190-011-0501-z.

Jazaeri, S., Amiri-Simkooei, A., Sharifi, M.A., 2014. On lattice reduction algorithms for solving weighted integer least squares problems: comparative study. GPS Solut. 18 (1), 105–114. https://doi.org/10.1007/s10291-013-0314-z.

Johnston, G., Riddell, A., Hausler, G., 2017. The International GNSS Service. In: Teunissen, P(eter) J.G., Montenbruck, O. (Eds.), Springer Handbook of Global Navigation Satellite Systems. Springer International Publishing, Cham, pp. 967–982. https://doi.org/10.1007/978-3-319-42928-133.

Kvas, A., Brockmann, J.M., Krauss, S., Schubert, T., Gruber, T., Meyer, U., Mayer-Gürr, T., Schuh, W.-D., Jäggi, A., Pail, R., 2021. GOCO06s–a satellite-only global gravity field model. Earth Syst. Sci. Data 13, 99–118. https://doi.org/10.5194/essd-13-99-2021.

Landskron, D., Böhm, J., 2018. VMF3/GPT3: refined discrete and empirical troposphere mapping functions. J. Geodesy 92 (4), 349–360. https://doi.org/10.1007/s00190-017-1066-2.

Laurichesse, D., Cerri, L., Berthias, J., Mercier, F., 2013. Real time precise GPS constellation and clocks estimation by means of a Kalman filter. In: Proceedings of the 26th international technical meeting of the satellite division of the Institute of Navigation (ION GNSS+ 2013), pp. 1155–1163.

Leick, A., Rapoport, L., Tatarnikov, D., 2015. GPS satellite surveying, fourth ed. John Wiley & Sons.

Li, B., Teunissen, P(eter) J.G., 2011. High dimensional integer ambiguity resolution: A first comparison between LAMBDA and Bernese. J.

Navig. 64 (S1), S192–S210. https://doi.org/10.1017/S037346331100035X.

Li, Z., Li, M., Shi, C., Fan, L., Liu, Y., Song, W., Tang, W., Zou, X., 2019. Impact of ambiguity resolution with sequential constraints on real-time precise GPS satellite orbit determination. GPS Solut. 23 (3), 1–14. https://doi.org/10.1007/s10291-019-0878-3.

Mahalanobis, P.C., 1936. On the generalized distance in statistics. In: Proceedings of the National Institute of Sciences of India. National Institute of Science of India.

Mayer-Gürr, T., Behzadpour, S., Eicker, A., Ellmer, M., Koch, B., Krauss, S., Pock, C., Rieser, D., Strasser, S., Süsser-Rechberger, B., Zehentner, N., Kvas, A., 2021. GROOPS: A software toolkit for gravity field recovery and GNSS processing. Comput. Geosci. 104864. doi: 10.1016/j.cageo.2021.104864.

Montenbruck, O., Steigenberger, P., 2020. GNSS orbit determination and time synchronization. Posit. Navig. Timing Technol. 21st Century: Integr. Satellite Navig. Sens. Syst. Civ. Appl. 1, 233–258. https://doi.org/10.1002/9781119458449.ch11.

Nardo, A., Li, B., Teunissen, P(eter) J.G., 2016. Partial ambiguity resolution for ground and space-based applications in a gps+ galileo scenario: a simulation study. Adv. Space Res. 57 (1), 30–45.

Odijk, D., Arora, B.S., Teunissen, P.J., 2014. Predicting the success rate of long-baseline gps galileo (partial) ambiguity resolution. J. Navig. 67 (3), 385–401. https://doi.org/10.1017/S037346331400006X.

Petit, G., Luzum, B., 2010. IERS conventions (2010). Technical Report Verlag des Bundesamts für Kartographie und Geodäsie.

Prange, L., Villiger, A., Sidorov, D., Schaer, S., Beutler, G., Dach, R., Jaggi, A., 2020. Overview of CODE's MGEX solution with the focus on Galileo. Adv. Space Res. 66(12), 2786–2798. doi: 10.1016/j.asr.2020.04.038. Scientific and Fundamental Aspects of GNSS - Part 1.

Rodriguez-Solano, C.J., 2009. Impact of albedo modelling on GPS orbits. M.Sc. thesis Technische Universität München. URL: https://mediatum.ub.tum.de/doc/1368717/file.pdf.

Rodriguez-Solano, C.J., 2014. Impact of non-conservative force modeling on GNSS satellite orbits and global solutions. Ph.D. thesis Technische Universität München. URL: https://mediatum.ub.tum.de/doc/1188612/file.pdf.

Steigenberger, P., Thoelert, S., Montenbruck, O., 2018. GNSS satellite transmit power and its impact on orbit determination. J. Geodesy 92 (6), 609–624. https://doi.org/10.1007/s00190-017-1082-2.

Strasser, S., Mayer-Gurr, T., 2021. IGS repro3 products by Graz University of Technology (TUG). Data set available at https://doi.org/10.3217/dataset-4528-0723-0867.

Strasser, S., Mayer-Gurr, T., Zehentner, N., 2019. Processing of GNSS constellations and ground station networks using the raw observation approach. J. Geodesy 93 (7), 1045–1057. https://doi.org/10.1007/s00190-018-1223-2.

Teunissen, P(eter) J.G., 1993. Least-squares estimation of the integer GPS ambiguities. Invited Lecture, Section IV Theory and Methodology, IAG General Meeting, Beijing, China. Also. In: Delft Geodetic Computing Centre LGR Series No. 6. Delft University of Technology.

Teunissen, P(eter) J.G., 1995. The least-squares ambiguity decorrelation adjustment: a method for fast GPS integer ambiguity estimation. J. Geodesy 70 (1), 65–82. https://doi.org/10.1007/BF00863419.

Teunissen, P(eter) J.G., 1998. Success probability of integer GPS ambiguity rounding and bootstrapping. J. Geodesy 72 (10), 606–612. https://doi.org/10.1007/s001900050199.

Teunissen, P(eter) J.G., 1999. An optimality property of the integer least-squares estimator. J. Geodesy 73 (11), 587–593. https://doi.org/10.1007/s001900050269.

Teunissen, P(eter) J.G., 2002. A new class of GNSS ambiguity estimators. Artif. Satellites 37 (4), 111–120.

Teunissen, P(eter) J.G., 2003a. Integer aperture GNSS ambiguity resolution. Artif. Satellites 38 (3), 79–88.

Teunissen, P(eter) J.G., 2003b. Towards a unified theory of GNSS ambiguity resolution. J. Glob. Position. Syst. 2 (1), 1–12.

Verhagen, S., Li, B., Teunissen, P(eter) J.G., 2012a. LAMBDA software package: Matlab implementation, version 3.0. Delft University of Technology and Curtin University, Perth, Australia.

Verhagen, S., Teunissen, P(eter) J.G., van der Marel, H., Li, B., 2011. GNSS ambiguity resolution: which subset to fix. In: IGNSS Symposium, pp. 15–17.

Verhagen, S., Tiberius, C., Li, B., Teunissen, P(eter) J.G., 2012b. Challenges in ambiguity resolution: biases, weak models, and dimensional curse. In: 2012 6th ESA Workshop on Satellite Navigation Technologies (Navitec 2012) & European Workshop on GNSS Signals and Signal Processing. IEEE, pp. 1–8.

Teunissen, P(eter) J.G., Massarweh, L., Verhagen, S., 2021. Vectorial integer bootstrapping: flexible integer estimation with application to GNSS. Journal of Geodesy 95 (99). doi: 10.1007/s00190-021-01552-2

Verhagen, S.A., 2004. The GNSS integer ambiguities: Estimation and validation. Ph.D. thesis Delft University of Technology.

Villiger, A., Dach, R., Schaer, S., Prange, L., Zimmermann, F., Kuhlmann, H., Wübbena, G., Schmitz, M., Beutler, G., Jäggi, A., 2020. GNSS scale determination using calibrated receiver and Galileo satellite antenna patterns. J. Geodesy 94 (9), 1–13. https://doi.org/10.1007/s00190-020-01417-0.

Zhang, F., 2006. The Schur complement and its applications, vol. 4. Springer Science & Business Media.